Nano Research

Open Access

Research Article

In-sensor processing enabled by monolithic dual-mode a-GaO_x/$Hf_{0.5}Zr_{0.5}O_2$ heterojunction for visual self-adaptation and anti-interference functionality

Weixu Hou[1], Jinhao Zhang[2], Yaju Zhang[1] ✉, Hao Xu[1], Weizhou Hou[1], Jingru Li[3], Qianqian Han[1], Yikun Li[1], Tianyu Wang[2] ✉, and Haiwu Zheng[1] ✉

[1] Henan Province Engineering Research Center of Smart Micro-nano Sensing Technology and Application, School of Physics and Electronics, Henan University, Kaifeng 475004, China
[2] School of Integrated Circuits, Shandong University, Jinan 250100, China
[3] School of Nanoscience and Materials Engineering, Henan University, Kaifeng 475004, China

Cite this article: *Nano Research*, **2026**, *19*, 94908926. https://doi.org/10.26599/NR.2026.94908926

ABSTRACT: The development of high-order neuromorphic computing requires device that integrates in-sensor visual sensing-memory-processing. However, integrated of volatile and non-volatile behavior, as well as reconfigurable architecture for antagonistic photoresponse—excitation and inhibition in single device under single-wavelength stimulus remains critical bottleneck in designing all-in-one neuromorphic visual system. Herein, an amorphous-GaO_x/$Hf_{0.5}Zr_{0.5}O_2$ (a-GaO_x/HZO) heterojunction device demonstrates dual-mode functionality switchover between sensing module (SM) and non-volatile module (NVM) by merely adjusting single-wavelength light intensity. The merit parameters of the SM are governed by switchable ferroelectric polarization, forming sufficient foundations for optoelectronic logic gates. The reconfigurable photoresponse—light intensity-dependent excitation and inhibition (i.e., Weber's Law) of the NVM endows the framework with visual self-adaptation, namely photopic and scotopic adaptation. Representative self-adaptation photosensitivity and adaptive index are strongly correlated with switchable ferroelectric polarization, thereby boosting responsiveness and self-adaptability. Leveraging the dual-mode switchover mechanism, the monolithic a-GaO_x/HZO heterojunction units integrated SM with NVM serve as sensing and computing building blocks for designing in-sensor processing: the SM with distinguishable photoresponse for pre-filtering of interference information and reconfigurable conductance of the NVM for performing anti-interference transmission of digits. This work provides a programmable framework for designing multimodal integrated neuromorphic vision chips and establishing brain-like sensory system for anti-interference communication.

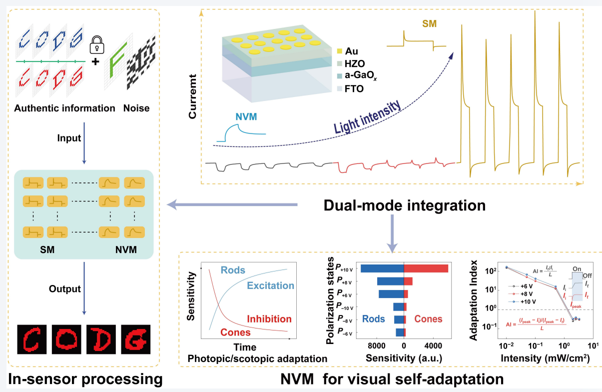

KEYWORDS: a-GaO_x/$Hf_{0.5}Zr_{0.5}O_2$ heterojunction, dual-mode functionality, non-volatile, ferroelectric polarization, in-sensor processing, self-adaptation

1 Introduction

Sensing module (SM) and non-volatile module (NVM) are two critical representational optoelectronic devices in communication, security management and imaging realms [1–5]. SMs have an advantage in performing rapid detection of light signals and transforming them into digital electrical outputs for information processing [6–8]. NVMs are superior in combining signal sensing, memory and processing [9–11]. On account of the inherent limitation in response speed of the NVM, the incorporation of a SM and an NVM is suitable for high-efficient neuromorphic system. Artificial visual sensor system (AVSS) holds unique qualities of monolithically integrating light signal sensing, data memory, and information processing [12, 13]. These sensing-

Received: February 1, 2026; **Revised:** June 6, 2026
Accepted: June 8, 2026

✉Address correspondence to Yaju Zhang, 40070002@vip.henu.edu.cn; Tianyu Wang, tywang@sdu.edu.cn; Haiwu Zheng, zhenghaiw@ustc.edu

memory-processing functions are commonly designed for physically separated units from conventional CMOS-based Von Neumann architecture [14]. To address the prevailing limitation in fabrication complexity, speed latency and energy consumption wall, bioinspired neuromorphic device offers a satisfactory alternative for miniaturization, high computing efficiency and low-power consumption, having emerging applications in multifunctional monolithic integrated device [15]. Thereby there is a growing demand for high-order integrated sensing and processing capabilities. The co-introduction of SM and NVM in a single device has emerged from simple hardware framework and dual-mode functionalities, which lays a solid sufficient foundation for establishing brain-like neural network [16, 17]. However, a switchover between SM and NVM in a single device remains a significant challenging on account of gap in response speed.

Recent research about photosensitive components of SM and NVM has primarily focused on low-dimensional materials [18], perovskites [19] and metal-oxide semiconductors [20]. Fang et al. developed a $Cs_3Sb_2I_9$-based dual-functional SM and NVM with visual sensing and memory capabilities [21]. Yan et al. proposed Bi_2SeO_5-based memristor that presented both fast response and synaptic characteristics by optoelectronic coupling stimulation [9]. However, these reported dual-functional devices were constrained by unipolar photoresponse and narrow spectral response range even under optical and electric dual stimuli. An emerging ultra-wide-bandgap semiconductor of gallium oxide (a-GaO_x) is noted for broad spectral response stemming from inherent oxygen vacancy (V_o) defects located at shallow- and deep-levels, showcasing promise for emulating integrated sensing and memristor characteristics [22–24]. Zhang et al. designed a $GaN/Ga_2O_3/GaN$ dual heterojunction device that demonstrated a switchover between SM and NVM by electrical mode actively tailoring the ionization and deionization processes of V_o defects [25].

In contrast to electrical stimulation mode faced with circuit complexity and interference, pure light stimulation mode holds marked advantages in non-contact operation, inherent crosstalk immunity and low-power consumption. Kim et al. developed a self-powered perovskite photodetector with a multilayer architecture that presented polarity switching of photocurrent—excitation and inhibition characteristics through multi-wavelength stimuli within a single device [26]. Nevertheless, prior studies relied on complex architecture and multi-wavelength illumination by either frequently changing light sources or employing optical filters [27–29]. The current challenge lies in how to realize antagonistic photoresponse—excitation and inhibition by applying a single-wavelength stimulus in a monolithic device. The ferroelectric component holding ferroelectric and pyroelectric polarization emerges for providing a programmable strategy to dynamically reconfigure photoresponse of neuromorphic devices [30]. Therefore, it is an urgent pursuit to develop neuromorphic devices for ultra-low power consumption, light-controlled sensing-processing integration and reconfigurable adaptive architecture.

Guided by this line of thought, we constructed a a-GaO_x/HZO heterojunction neuromorphic device featuring dual-mode functionality of SM and NVM. The sensitivity and detectivity of the SM is fine-tuned by switchable ferroelectric polarization, enabling two optoelectronic logic gates. The NVM demonstrates antagonistic photoresponse—excitation and inhibition changing with light intensity, namely Weber's Law. Representative self-adaptation photosensitivity and adaptive index during photopic and scotopic adaptation processes are modulated by switchable ferroelectric polarization attribute, allowing for high responsiveness and adaptability. On basis of distinguishable photoresponse to red-green-blue (RGB) wavelengths, the SM is adept at preprocessing interference information and then the reconfigurable conductance pathways of the NVM are employed to construct monolithically integrated in-sensor processing system targeting anti-interference communication.

2 Results and discussion

2.1 Conceptual idea and characterization of a-$GaO_x/Hf_{0.5}Zr_{0.5}O_2$ heterojunction neuromorphic device

Adaptation is a defining attribute by which organisms dynamically alter their responses adapt to real-time changing environmental stimuli. Visual self-adaptation, as one of indispensable adaptation activities, empowers biological visual system to precisely discriminate the dynamical shifting of light intensity prevalent in natural environments [31–34]. The visual sensing and self-adaptation of the human retina are supported by a network composed of specialized cells, primarily including photoreceptor cells (rod cells and cone cells) and horizontal cells (Fig. 1(a)). The clear division of photoreceptor tasks is to assign rod and cone cells to percept and make an activity of dim/high illumination, spanning the range of the organism's response to different background intensities [35, 36]. The fundamental principle that their perceived sensitivity is inversely proportional to background light intensity is known as Weber's Law (Fig. 1(b)). An alternative description of Weber's law is that the visual threshold of the retina monotonically increases with increasing background intensity (Fig. S1 in the Electronic Supplementary Material (ESM)).

The visual self-adaptation involves two processes: scotopic adaptation from bright to dim scene and photopic adaptation from dim to bright scene. Taking a vehicle driver passing through a tunnel as example, the drivers are initially blind when they enter a dark tunnel from a bright environment and then gradually recognize objects during scotopic adaptation process. This is because the sensitivity of the retina gradually increases over time (Fig. 1(c)). Photopic adaptation is the essential reversal of scotopic adaptation. When drivers exit the dark tunnel and enter a bright environment, they are temporarily dazzled upon sudden exposure to a high-intensity scene and then gradually adapts to bright scene during photopic adaptation process, which arises from a gradual decrease of retina sensitivity over time (Fig. 1(d)). In addition, the visual system also demonstrates a distinct responsivity to RGB wavelengths over visible spectral range. When a certain wavelength evokes a pronounced response in the synaptic device, it is called a photosensitive wavelength. Otherwise, non-sensitive wavelength is characterized by a low sensitivity in response to light illumination. Inspired by biological retinal system, a critical architecture unit—neuromorphic device is expected to hold visual self-adaptation and spectral discriminability. These discriminable responsivities to RGB tricolor wavelengths of neuromorphic device are intended for conducting anti-interference transmission of visual information (Fig. 1(e)). The input process is described as follows: The photosensitive wavelength encodes authentic information, while the non-sensitive wavelength carries interference noise. The combined input is pre-processed to filter out interference noise based on discriminable responsivities of the expected

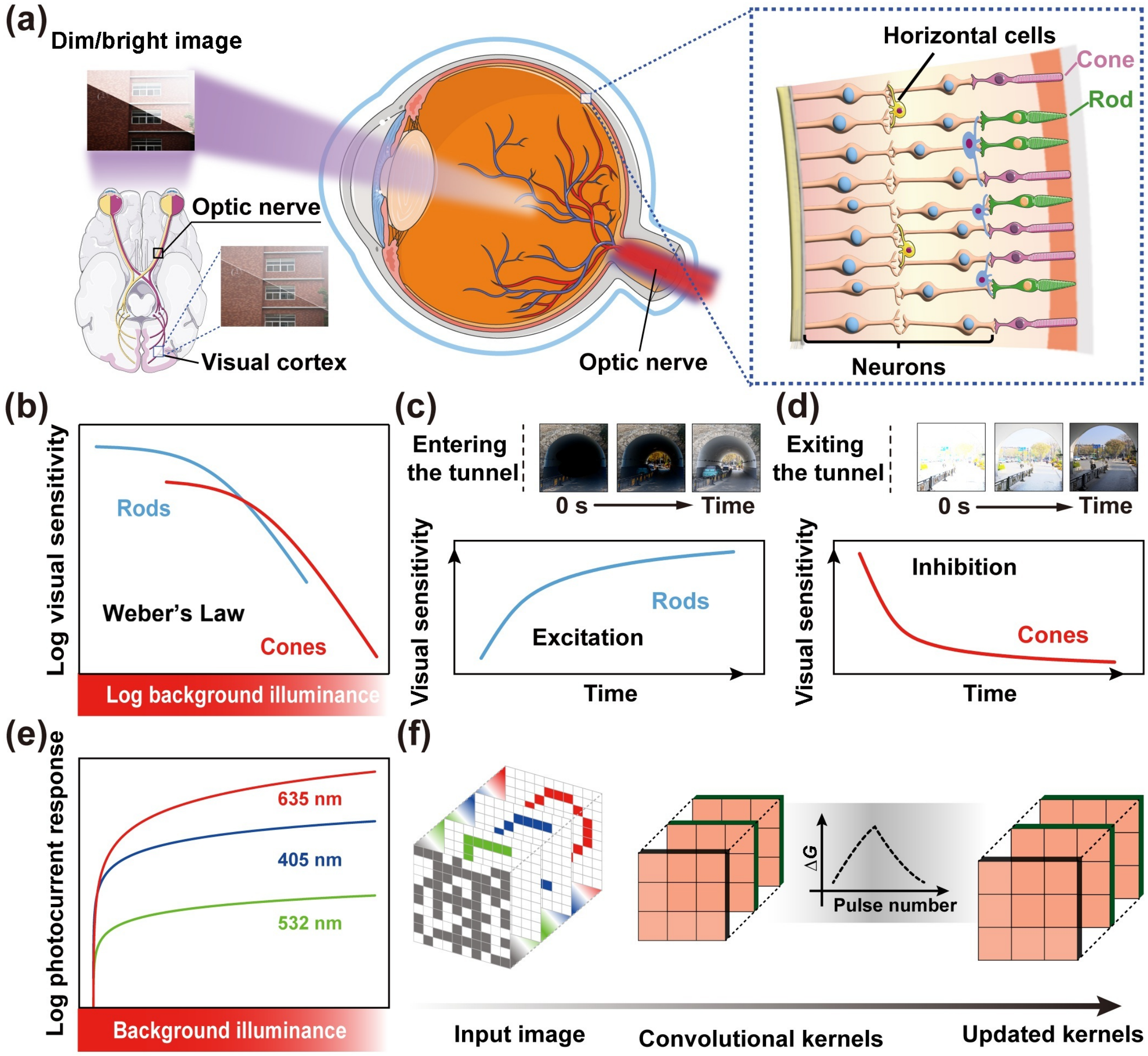

Figure 1 (a) The retina composed of cone and rod photoreceptors and horizontal cells adapting to dim-/high-illumination perception. (b) Weber's Law: a fundamental principle of the visual sensitivity of cones and rods being inversely proportional to light stimuli. (c) Photopic adaptation process of the retina during entering the tunnel: light intensity dependent photoresponse excitation of rod cells. (d) Scotopic adaptation process of the retina during exiting the tunnel: light intensity dependent photoresponse inhibition of cone cells. (e) The photocurrent response versus light intensity under multi-wavelength illumination. (f) Anti-interference transmission performed by the artificial neural network (ANN).

neuromorphic device and then can be recognized by an artificial neural network (ANN) based on monolithically integrated unit, as shown in Fig. 1(f).

Guided by this objective, the GaO_x/HZO heterojunction neuromorphic device is constructed as a fundamental unit for AVSS, as shown in Fig. 2(a). Detailed introduction for device preparation procedures and morphological characterization are provided in the Experimental section and Figs. S2 and S3 in the ESM. The root mean square (RMS) roughness of the GaO_x and HZO films was characterized by the atomic force microscopy (AFM) at the nanoscale, indicating high-quality growth of the GaO_x and HZO films (Figs. S2(b) and S2(c) in the ESM). From X-ray diffraction (XRD) patterns of pure GaO_x film and GaO_x/HZO heterojunction (Fig. S2(d) in the ESM), no obvious diffraction peaks attributable to crystallization phase are observed, indicating the formation of amorphous GaO_x (a-GaO_x). Combined with grazing incidence X-ray diffraction (GIXRD) characterization of the heterojunction (Fig. S2(e) in the ESM), there is a prominent diffraction peak at $2\theta = 30.5°$, corresponds to orthorhombic (111) and tetragonal (011) mixed-phases of the HZO layer. The presence of orthorhombic phase in the HZO layer contributes to ferroelectricity [37], providing a programmable platform for tailoring photoresponse characteristics of the a-GaO_x/HZO heterojunction.

Ferroelectric polarization switching in the HZO layer was further investigated by piezoresponse force microscopy (PFM) (Fig. 2(b)). There is approximately 180° phase contrast between upward and downward polarization regions by respectively applying −10 and +10 V. This result is consistent with the PFM hysteresis loop and butterfly-shaped amplitude curve (Fig. S2(f) in the ESM), indicating switchable polarization characteristics of the HZO layer. Previous numerous studies have introduced switchable ferroelectric polarization-controlled depolarization field to act on the separation and transport processes of photogenerated carriers, offering a

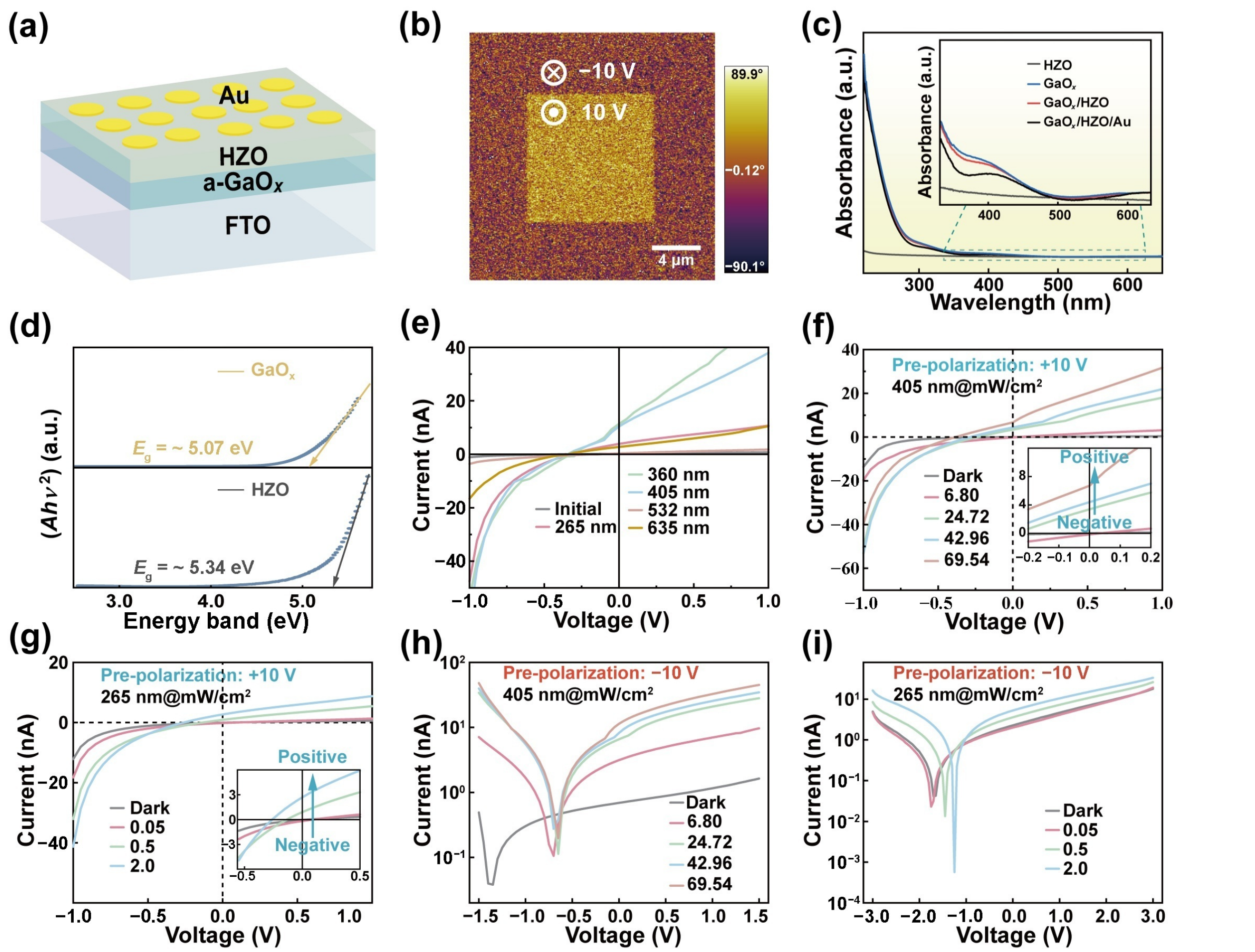

Figure 2 Structure and characterization of a-GaO$_x$/HZO heterojunction device. (a) Schematic of the a-GaO$_x$/HZO heterojunction. (b) PFM out-of-plane phase-contrast image of the HZO film. (c) Optical absorption spectra of HZO and a-GaO$_x$ components and a-GaO$_x$/HZO heterojunction device (the inset presents a magnified view of the device's optical absorption over the wavelength range of 350–620 nm). (d) The bandgap fitting plots of HZO and a-GaO$_x$ components. (e) The *I*–*V* characteristics under 265, 360, 405, 532, and 635 nm light illumination. The *I*–*V* characteristics of the $P_{+10\,V}$-state device under (f) 405 nm and (g) 265 nm illumination (the inset presents the photoresponse of the $P_{+10\,V}$-state device and light intensity under 405 nm and 265 nm illumination). The *I*–*V* characteristics of the $P_{-10\,V}$-state device under (h) 405 and (i) 265 nm illumination.

feasible solution for regulating the photoresponse of ferroelectric heterojunctions [38–41].

To evaluate the potential as a photosensitive heterojunction device, the ultraviolet–visible (UV–Vis) transmittance and absorption spectra of HZO component, a-GaO$_x$ component, a-GaO$_x$/HZO heterojunction devices with and without Au electrode as well as a-GaO$_x$/HZO heterojunction device fully covered with Au film are performed and illustrated in Figs. S2(g) and S2(h) in the ESM and Fig. 2(c). The a-GaO$_x$ component demonstrates primary absorption over solar-blind UV and visible range, while HZO component exhibits high transmittance from UV to visible range. Specially, the a-GaO$_x$ component displays a steep absorption edge located at near 280 nm and extended absorption wavelength range 300–700 nm, which is consistent with that of the a-GaO$_x$/HZO heterojunction devices. Extended absorption range of the a-GaO$_x$ component and the a-GaO$_x$/HZO heterojunction device may be originated from the introduction of sub-bandgap levels associated with intrinsic V$_o$ defects in the a-GaO$_x$. Based on the Tuac formula, the optical bandgaps of a-GaO$_x$ and HZO components are determined to be approximately 5.07 and 5.34 eV as shown in Fig. 2(d), respectively.

The defect concentration of V$_o$ was quantitatively calculated using the O 1s core-level X-ray photoelectron spectroscopy (XPS) of the a-GaO$_x$ component. From Fig. S2(i) in the ESM, two sub-peaks corresponding to lattice oxygen (O$_I$) and oxygen vacancy (O$_{II}$) are observed. The O$_{II}$/(O$_{II}$ + O$_I$) ratio is calculated as about 20% by the Gaussian fitting, implying high-concentration V$_o$ defects in the a-GaO$_x$ component. According to previous reports, V$_o$ defect engineering endows oxide semiconductors such as ZnO [42], IGZO [43] and GaO$_x$ [44] with persistent photoconductivity (PPC) phenomenon by governing the trapping/detrapping behaviors of photo-generated carriers, establishing the cornerstone for developing bandgap-oxide based NVM. The band alignment at the a-GaO$_x$/HZO heterointerface is specifically characterized by combining XPS and ultraviolet photoelectron spectroscopy (UPS) measurements (Fig. S4 in the ESM). Through detailed analysis (Note S1 in the ESM), a typical II-type band alignment is formed at the heterointerface between a-GaO$_x$ and HZO layers, ensuring the effective photogenerated carriers' separation and transport at a-GaO$_x$/HZO heterointerface. Therefore, the a-GaO$_x$/HZO heterojunction with II-type band alignment is suitable for highly photosensitive devices.

Building on extended absorption capability from solar-blind UV to visible range and II-type band alignment, the heterojunction device manifests broad band self-powered photoresponse under 265, 360, 405, 532, and 635 nm illumination as shown in Fig. 2(e). From the current–voltage (I–V) characteristics, the photoresponse of the device under short-wavelength illumination of 265, 360, and 405 nm is significantly pronounced compared with under long-wavelength 532 and 635 nm illumination.

To investigate the influence of ferroelectric polarization state on the photoresponse of the device, −10, −8, −6, +6, +8 and +10 V bias were applied to the device to obtain upward polarization states $P_{-10\ V}$, $P_{-8\ V}$, $P_{-6\ V}$ and downward polarization states $P_{+6\ V}$, $P_{+8\ V}$ and $P_{+10\ V}$, respectively. During the testing procedure, the device was illuminated by either a 405 nm laser (ranging from 6.80 to 69.54 mW/cm^2) or 265 nm LED (ranging from 0.05 to 2.00 mW/cm^2). Figures S5 and S6 in the ESM comprehensively plot the dependence of I–V characteristic of the heterojunction device on a diverse of ferroelectric polarization states $P_{-10\ V}$, $P_{-8\ V}$, $P_{-6\ V}$, $P_{+6\ V}$, $P_{+8\ V}$, and $P_{+10\ V}$. As representative examples, under the $P_{+10\ V}$ state, it is notable that the polarity switching of both the short-current (I_{sc}) and open-circuit voltage (V_{oc}) extracted from Fig. 2(f) and Fig. S5(f) in the ESM is demonstrated as light intensity increasing under 405 nm illumination, that is, the I_{sc} shifts from negative to positive, as shown in the insert of Fig. 2(f). Similarly, the $P_{+10\ V}$-state device demonstrates outstanding photoresponse polarity-switching characteristics under 265 nm illumination (Fig. 2(g)). Specifically, it can be observed that the I_{sc} of the $P_{+10\ V}$-state device shifts from negative magnitude of −0.06 nA toward positive magnitude of 4.59 nA, while V_{oc} changes from positive magnitude of 0.05 V toward negative positive magnitude of −0.35 V as light intensity increases, as shown in Fig. 2(g). Figures 2(h) and 2(i) present that the positive I_{sc} of the $P_{-10\ V}$-state device increases with increasing light intensity regardless of whether under 405 or 265 nm illumination, while the negative V_{oc} decreases.

The polarity of photocurrent as a function of ferroelectric polarization state is statistically analyzed and plotted in Fig. S7 in the ESM. The polarity of I_{sc} of the device shifts from positive to negative by switching from negative to positive polarization states under weak intensity illumination (0.05 mW/cm^2). These results provide compelling evidence that enhanced ferroelectric polarization is responsible for optimizing photoresponse and switchable ferroelectric polarization serves as a pragmatic approach to implement photoresponse excitation and inhibition characteristics. The magnitude and polarity of photoresponse of the heterojunction device with II-type band alignment is closely correlated with the cooperative and competitive mechanism [45–47]. A detailed explanation will be provided in following sections.

2.2 The switchover between non-volatile module and sensing module for Morse code and logic gates

The comprehensive photocurrent–time (I–T) curves of the a-GaO_x/HZO heterojunction device are further performed under 405/360 nm illumination and $P_{-10\ V}$/$P_{+10\ V}$ states. Figure S8 in the ESM demonstrates an obvious four-stage dynamic photoresponse of the device for each light pulse cycle under $P_{-10\ V}$ state and 405 nm illumination. Taking one cycle as an example (Fig. S9 in the ESM), when light pulse is on or off for a period, only dark current (I_{dark}) is present in stage I, and a steady photocurrent (I_s) is induced by the coupling of ferroelectric polarization with the optoelectrical effect (the ferro-optoelectrical effect) in stage III. Once light pulse on (stage II) or off (stage IV), a transient spike of photocurrent (I_{peak}) emerges because of the coupling of ferroelectric and pyroelectric polarization with the optoelectrical effect (the ferro-pyro-optoelectrical effect). This typical phenomenon has been verified in our previous work and other studies, and has been employed to improve photoresponse of the a-GaO_x/HZO heterojunction device [48–51]. As light intensity increases, both I_s and I_{peak} present an increase trend. These characteristics demonstrate that the device is suitable as a SM.

From Figs. 3(a) and 3(b), the photoresponse behaviors of the device in the $P_{+10\ V}$ state is significantly is distinguished from the SM when the device is in the $P_{-10\ V}$ state (Fig. S8 in the ESM) regardless of whether the wavelength is 360 or 405 nm. As the light intensity increases, the photocurrent polarity of the device switches from negative to positive, accompanied by the transition between non-volatile and volatile behaviors. In particular, the subsequent negative photocurrent is lower than the prior one under 405 nm light illumination with weak intensity below 6.8 mW/cm^2 due to the PPC phenomenon, as illustrated in the right panel of Fig. 3(b). In this case, the non-volatile nature of the device allows it for becoming an NVM. When light intensity increases beyond 6.8 mW/cm^2, the photocurrent behavior evolves from non-volatile and volatile response and the photocurrent polarity of the device shifts from negative to positive, enabling the single a-GaO_x/HZO heterojunction device to play dual roles as an NVM and a SM. Similarly, robust bipolar and dual-mode characteristics of the device dependent on light intensity were also observed under $P_{+6\ V}$ and $P_{+8\ V}$ states (Fig. S9 in the ESM).

The outstanding bipolar photoresponse and dual-mode switchover mechanism between SM and NVM roles is governed by the ferro-pyroelectrical effect. Two competing photoinduced processes between ionization ($V_o - e \rightarrow V_o^+/V_o^{2+}$) and deionization ($V_o^+/V_o^{2+} + e \rightarrow V_o$) have emerged due to the presence of abundant inherent V_o defects in the a-GaO_x component. As illustrated in Fig. S10 in the ESM, when the $P_{+10\ V}$-state device is illuminated by weak intensity, the transformation process from initial V_o to V_o^+/V_o^{2+} ionized states releases electrons, whereas the limited number of photogenerated electrons inhibits the deionization process. Therefore, these positively charged V_o^+/V_o^{2+} states are generated by the ionization process rather than the deionization process and act as electron traps, resulting in a non-volatile photocurrent. On the other hand, the depolarization field ($E_{dp\text{-}up}$) is in the opposite direction to the built-in electric field (E_{bi}) and the $E_{dp\text{-}up}$ exceeds the E_{bi}, consequently generating a negative photocurrent. Under strong intensity illumination, accumulated photogenerated electrons are conductive to the deionization process of V_o^+/V_o^{2+}, leading to a negligible number of ionized states. In this case, the device presents volatile characteristics because of the lack of carrier trapping sites. Furthermore, strong light exposure causes ferroelectric polarization to degenerate due to a significant increase in temperature (Figs. S11–S15 in the ESM). Correspondingly, the $E_{dp\text{-}up}$ diminishes below the E_{bi}, leading to a reverse photocurrent.

Building upon non-volatile characteristics under weak intensity, the role of NVM paves the way for emulating Morse codes encoding. International Morse codes, a standardized wireless communication protocol, ensures the transmission of alphanumeric characters and punctuation symbols (Fig. S16 in the ESM). Compared with conventional Morse codes reliant on pressure-sensing mechanism, the light-pulse modulated Morse codes have superior stability and reproducibility in non-destructive and contactless operation. Firstly, a signal encoding protocol was defined as: Morse code elements "·" (dot) and "—" (dash line) were

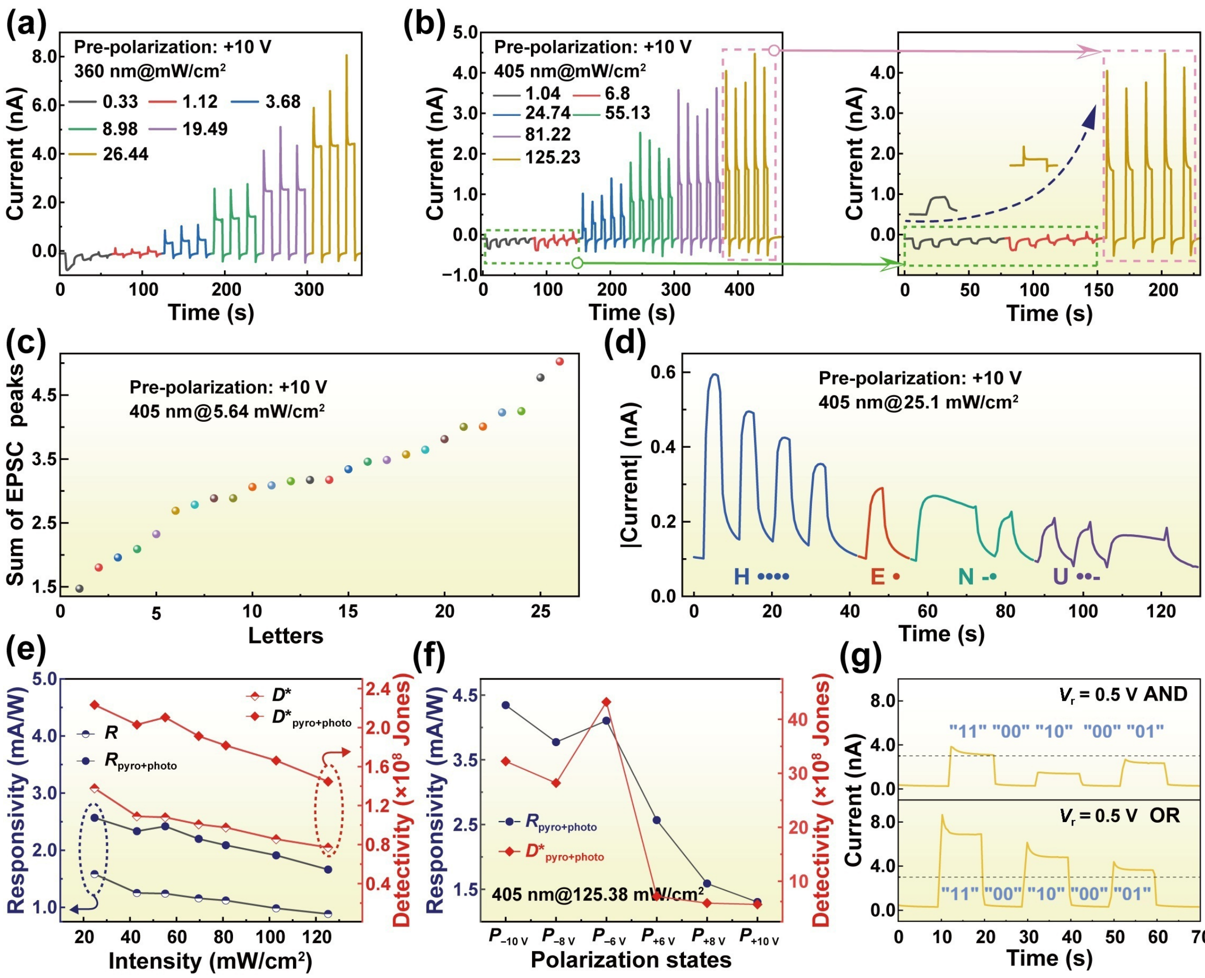

Figure 3 Visible photoresponse characteristics of the heterojunction device. The *I*–*T* curves of the $P_{+10\,V}$-state device under (a) 360 and (b) 405 nm illumination. (c) The Morse codes compilation and transmission of 26 English alphabets. (d) The real-time Morse encoding of "HENU". (e) The R, D^*, $R_{pyro+photo}$ and $D^*_{pyro+photo}$ values of the SM under 405 nm illumination. (f) The $R_{pyro+photo}$ and $D^*_{pyro+photo}$ values of the SM dependent on polarization states under 405 nm illumination. (g) AND and OR optoelectronic logic gates (OELGs) based on the $P_{+10\,V}$-state device (V_{read} = 0.5 V).

respectively represented by a short pulse (pulse duration of 4 s) and a long pulse (pulse duration of 15 s) of weak intensity (5.64 mW/cm²). Owing to non-volatile characteristics of the NVM, a sequence of light pulses can evoke multi-state amplitudes of photocurrent and 26 sequences of light pulse can generate 26 distinct amplitude states. Correspondingly, the compilation and transmission of the Morse codes for 26 English alphabets are demonstrated in Fig. 3(c) and Fig. S17 in the ESM. Figure 3(d) displays real-time Morse encoding of the "HENU" character string based on the inherent nonlinear photoresponse dynamics of the NVM. In terms of photoresponse induced by different sequences of light pulses, the NVM demonstrates the potential feasibility of neuro-inspired optical wireless communication for human-machine interfaces.

Thanks to the volatile photoresponse, the SM is capable of rapidly responding to light stimuli. Response time of the SM, a critical performance metric, as shown in Fig. S18 in the ESM. The rise and decay times were defined as the time intervals to increase from 10% to 90% and decrease from 90% to 10% of the maximum photocurrent, respectively. The a-GaO_x/HZO heterojunction SM exhibits relatively short rise time of 13.38 ms and decay time of 10.12 ms compared with other a-GaO_x-based devices [23, 44, 52–55]. Responsivity (R) reflects sensitivity response of the SM to light stimuli and detectivity (D^*) refers to the capability for detecting weak light signal. Merit parameter of R and D^* is calculated as Eqs. (1) and (2)

$$R = \frac{I_{light} - I_{dark}}{L \times A} \tag{1}$$

where L denotes light intensity, A is the active area of the device and I_{light} represents the photocurrent induced by different light intensities. To accurately evaluate the D^* of the photoelectric device, the noise power spectral density (S_n) of the a-GaO_x/HZO heterojunction device is measured in the frequency range from 0.01 to 10 Hz, as shown in Fig. S19 in the ESM. Over the frequency range from 0.01 to 10 Hz, the noise spectral density exhibits a clear frequency-dependent behavior: it increases with decreasing frequency, and follows an inverse-frequency relationship. This is a hallmark of 1/f noise, rather than thermal noise or shot.

$$D^* = \frac{R\sqrt{A}}{S_n} \tag{2}$$

The S_n is extracted at a 1 Hz bandwidth under different polarization states. The corresponding R/D^* and $R_{pyro+photo}$/$D^*_{pyro+photo}$ are calculated using the I_s value and the average value of I_{peak}

Tsinghua University Press | SciOpen

extracted from the multicycle measurements in Fig. S8(a) in the ESM. As revealed in Fig. 3(e), all of the R, D^*, $R_{pyro+photo}$ and $D^*_{pyro+photo}$ values of the SM demonstrate decreasing trends with increasing light intensity. The maximum values of the R, D^*, $R_{pyro+photo}$ and $D^*_{pyro+photo}$ are 1.58 mA/W, 1.38 × 10^8 Jones, 2.57 mA/W and 2.23 × 10^8 Jones, respectively. These results that the ratios of $R_{pyro+photo}/R$ and $D^*_{pyro+photo}/D^*$ are respectively as high as 163% and 162% underlines the ferro-pyro-optoelectrical effect in enhancing the performance metrics of the SM. Moreover, the $R_{pyro+photo}$ and $D^*_{pyro+photo}$ of the SM are highly dependent on the ferroelectric polarization states, as statistical summarized in Fig. 3(f). The maximums of $R_{pyro+photo}$ and $D^*_{pyro+photo}$ are 4.34 mA/W and 3.82 × 10^9 Jones, respectively, indicating that switchable ferroelectric polarization is a flexible and efficient approach for optimizing signal detection capability of the SM.

Based on its rapid high photosensitivity, the SM-based optoelectronic logic gates (OELGs) are modulated via the synergistic control of wavelength and intensity by setting read voltage as 0.5 V. Figure S20 in the ESM schematically illustrates two elementary OELGs (AND and OR) according to the truth table covering the input-output Boolean relationships. The light input signals "A" and "B" respectively represent 405 and 360 nm wavelength and the input states "1" and "0" respectively denote the presence and absence of light signal. A corresponding output current below the threshold of 3 nA is defined as a logic "0", while a current exceeding the threshold of 3 nA is assigned as a logic "1". As specified above, the "AND" OELG is schematically demonstrated in Fig. 3(g) (upper panel) when the SM is simultaneously illuminated by 405 (76.99 mW/cm^2) and 360 nm (10.66 mW/cm^2) light. A photocurrent of the SM remains below the threshold if either input A or input B is applied alone, producing a logic output "0". When both inputs A and B are present, a photocurrent of the SM above the threshold is generated, yielding a logic output "1".

The other "OR" OELG is schematically illustrated in Fig. 3(g) (lower panel) under simultaneous illumination with 405 (110.35) and 360 nm (25.38 mW/cm^2) light. In the absence of both inputs A and B, a photocurrent of the SM is below the threshold, signifying a logic output "0". When one or both of the inputs A and B are present, the photocurrent of the SM exceeds the threshold, representing a logic output "1". The power consumption of individual "AND" or "OR" OELG event is evaluated as low as 3.53 and 7.82 nW (Table S1 in the ESM), respectively, becoming one of state-of-the-art approaches compared with existing alternatives [56, 57]. These OELGs offer a significant advantage over conventional CMOS in terms of power efficiency, positioning them as promising candidate for next-generation neuromorphic processing.

2.3 Visual self-adaptation of the neuromorphic device based on the non-volatile module

Since the photosensitivity of the a-GaO_x/HZO heterojunction extends human vision into the solar-blind region (Fig. 2(c)), the dynamic photoresponse characteristics of the device with $P_{+10\,V}$ state is conducted under 265 nm light illumination with a large range of intensities, as plotted in Fig. 4(a). When exposed to weak light, the device only demonstrates a gradual increase of I_s, which is dominated by the ferro-optoelectrical effect. With increasing light intensity, the transient I_{peak} induced by the ferro-pyro-optoelectrical effect emerges and then decays. Moreover, the device under different $P_{+8\,V}$, $P_{+6\,V}$, $P_{-6\,V}$, $P_{-8\,V}$, and $P_{-10\,V}$ states demonstrate similar photoresponse characteristics (Fig. S21 in the ESM). Notably, the device manifests distinguishable photoresponse under weak and strong intensity illumination, from which two representative cases are illustrated in Fig. 4(b). Under weak intensity of 20.0 μW/cm^2 illumination, the magnitude of the I_s gradually increases due to the PPC phenomenon (Fig. 4(b), upper panel). In contrast, the magnitude of the I_{peak} decays rapidly under strong intensity of 3.0 mW/cm^2 illumination (Fig. 4(b), lower panel). The gradual enhancement and attenuation trend of the device's photocurrent ensures that the dual effects of excitation and inhibition can be achieved merely by adjusting single-wavelength light intensity. These experimental results provide a conclusive proof that single-wavelength stimuli can trigger antagonistic photoresponse—excitation and inhibition in a single device, laying essential groundwork for simulating visual self-adaptation based on the neuromorphic device.

Drawing inspiration from the self-adaptation dynamics of biological photoreceptors, the photosensitivity parameter of the device can be utilized as a metric for evaluating its adaptability over a broad range of light intensities. The photosensitivity (S) is mathematically represented as Eq. (3)

$$S = \frac{\Delta I}{L} = \frac{I_0 - I_t}{L} \tag{3}$$

where ΔI is the photocurrent variation, I_t denotes the photocurrent at time t and I_0 represents the current at time t = 0 s [31, 32]. Figure S22 in the ESM plots the dependence of S on L, in which the inverse dependence of S on L signifies a cornerstone model in sensory psychology. It follows Weber's Law and provides a quantitative prediction for detection range, defined as Eq. (4)

$$\frac{S}{S_0} = \frac{L_0}{L_0 + L} \tag{4}$$

where S_0 denotes the dark-state sensitivity and L_0 represents the light intensity at half-maximum photosensitivity [31, 32, 36]. The linear relationship curve in Fig. 4(c) is composed of two linear branches. One branch describes the S within weak intensity range of 0.01–0.10 mW/cm^2, corresponding to rods-like scotopic adaptation. S_0 and L_0 are respectively estimated as 12,620 and 5.5 × 10^{-2}. Another branch describes the S over strong intensity range of 0.5–3.3 mW/cm^2, aligning with cones-like photopic adaptation. The fitting S_0 and L_0 are respectively estimated as 6024 and 22.2 × 10^{-2}. To assess the detection threshold for the difference in light intensity that the visual system can perceive, the visual threshold ΔL is introduced as $\Delta L = 1/S$. The ΔL increases with increasing L and a logarithmic-scale slope of k is extracted as 0.92. A robust proportional relationship between ΔL of the device with $P_{+6\,V}$, $P_{+8\,V}$, $P_{+10\,V}$ states and L is analogous to biological retinal photoreceptors (Fig. S23 in the ESM).

To detailly describe the visual self-adaptation characteristics of the neuromorphic device, Fig. 4(d) delineates the magnified I–T curves under different light intensities. The neuromorphic device exhibits photocurrent excitatory under weak intensity illumination ranging from 10 to 100 μW/cm^2. Conversely, when illuminated by strong intensity across 0.5–3.3 mW/cm^2, the device showcases distinct photocurrent inhibition. Similar phenomena of photocurrent excitatory and inhibition are confirmedly observed when the device is set at different polarization ($P_{+6\,V}$, $P_{+8\,V}$, $P_{-6\,V}$, $P_{-8\,V}$, and $P_{-10\,V}$) states as indicated by Figs. S24 and S25 in the ESM. This consistent antagonistic photoresponse behavior-excitation and inhibition of the neuromorphic device provides a solid cornerstone for mimicking visual self-adaptation by simple adjusting single-

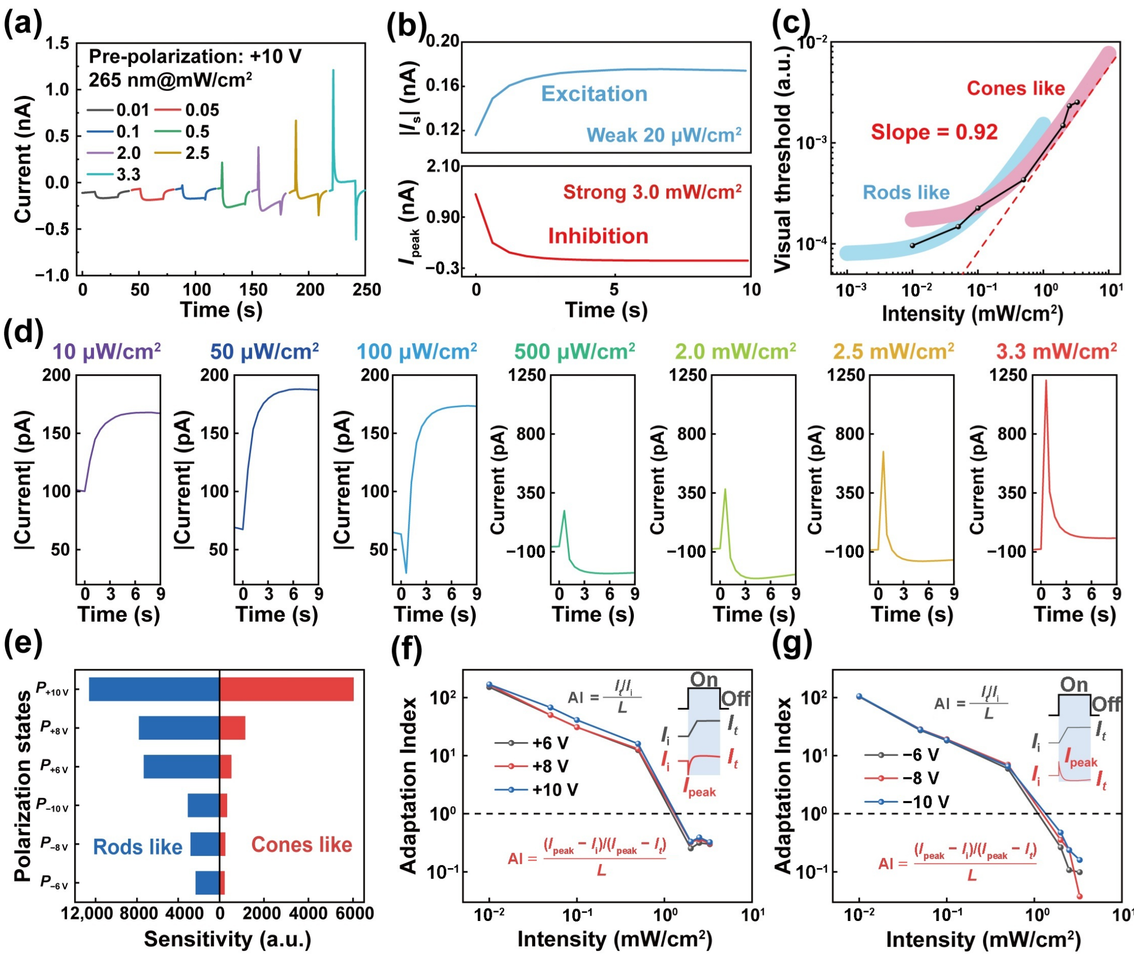

Figure 4 Dynamic photocurrent characteristics of the NVM. (a) The *I*–*T* curves of the NVM under different light intensities with 265 nm illumination. (b) Dynamic photocurrent characteristics of the NVM under weak intensity (20.0 μW/cm²) and strong (3.0 mW/cm²) intensity of 265 nm illumination. (c) The visual threshold as a function of background intensity. (d) The magnified *I*–*T* curves of the NVM under different light intensities. (e) The extracted correlation between sensitivity (*S*) and polarization state across weak and strong light intensities. The adaptive index (AI) as a function of light intensity under (f) downward polarization states and (g) upward polarization states.

wavelength light intensity. Moreover, switchable ferroelectric polarization has been identified as a critical factor for the self-adaptation photosensitivity in adapting to real-time-varied background intensity. Figure 4(e) displays the extracted correlation between *S* and polarization state across weak and strong intensities. The *S* value of the neuromorphic device significantly increases with switching ferroelectric polarization from $P_{-6\text{ V}}$ to $P_{+10\text{ V}}$ state. Specifically, dynamic rods-and cones-like photosensitivity ranges are up to 5.48 and 26.77 by calculating the ratios of maximum to minimum photosensitivity, respectively, indicating that switchable ferroelectric polarization enables effective modulation of responsiveness during visual self-adaptation process.

For deeper insight into photo-adaptive characteristics, the adaptive index (AI) is introduced as a quantitative metric to estimate the effect of light intensity on photocurrent weight, which is defined by the following expression (Eqs. (5) and (6)) [58]

$$\mathrm{AI} = \frac{I_t/I_i}{L} \quad (5)$$

$$\mathrm{AI} = \frac{(I_{peak} - I_i)/(I_{peak} - I_t)}{L} \quad (6)$$

where I_i denotes the initial dark current. As can be seen from Figs. 4(f) and 4(g), the AI of the neuromorphic device exceeds the threshold of 1 under weak light illumination, representing the emergence of photocurrent excitatory behavior. In contrast, the AI of the neuromorphic device falls below the threshold of 1 under strong light illumination, corresponding to photocurrent inhibition behavior. Furthermore, the neuromorphic device demonstrates consistent self-adaptability regardless of polarization states, highlighting the robustness of the single-wavelength intensity modulation strategy.

2.4 In-sensor processing based on a-GaO_x/$Hf_{0.5}Zr_{0.5}O_2$ heterojunction for anti-interference functionality

Inspired by information processing mechanism of the human brain, compared with the traditional separation of sensing, transmission and processing units, the core of in-sensor processing lies in "perception-as-processing". Within this framework, the sensing unit can not only convert external stimuli into output signals, but also pre-process the input signals through *in-situ* filtering and computation. This paradigm requires the neuromorphic device to filter out background interference and then encode authentic information in a manner analogous to that of a biological retina. Building on this concept, the a-GaO_x/HZO heterojunction neuromorphic device is expected to become an ideal candidate for integrated sensing-memory-processing due to its dual roles as a SM and an NVM. It is worth noting that this device does not aim to optimize photoelectric detection or in-sensor computing alone, but rather the integration between the two functions. The photosensitivity characteristics of the SM were investigated under visible light illumination. By extracting data from *I*–*V* curves of the SM under $P_{+10\ \mathrm{V}}$ state and 405/532/635 nm illumination (Figs. S4(f) and S26 in the ESM), the SM showcases significantly enhanced photoresponse evoked by either 405 or 635 nm light illumination compared with 532 nm light illumination in Fig. 5(b). On the basis of distinguishable photoresponse to RGB wavelengths, the SM is notable for filtering green light signal interference to carry out pre-processing. Figure S27 in the ESM schematically illustrates the dedicated SM for detecting the authentic Modified National Institute of Standards and Technology (MNIST) digits (Figs. S28 and S29 in the ESM), where the expected information carried by the blue- and red-light signals is interleaved with the interference of the green light signal. When mixed light signals are captured by the SM, both the blue- and red-light signals induce a pronounced photoresponse, while the response to green light signal is negligible. After the pre-process, such pre-filter interference of mixed information is beneficial for enhancing subsequent pattern recognition accuracy and low-power consumption, as illustrated in Fig. 5(a).

To perform the recognition of authentic digital information, an ANN was constructed by capitalizing on the reconfigurable conductance pathways of the NVM. The NVM-based ANN is composed of 784 input neurons, 100 hidden neurons and 10 output neurons. The digital recognition task performed by the ANN relies on the potentiation and depression conductance states of the NVM. Figure S30 in the ESM offers the long-term conductance potentiation (LTCP) and long-term conductance depression (LTCD) behaviors of the NVM by a mixture of optical and electrical pulse stimulation. The conductance of the NVM progressively increased under 27 stimulus sets (each set: one poling voltage pulse followed by one light pulse, Fig. S31 in the ESM), whereas it gradually decreased under 27 consecutive electrical pulses. During LTCP stage, every conductance is extracted by averaging the photocurrent over ten consecutive cycles (Fig. S30(a) in the ESM). An overall conductance state of 54 reveals good conductivity adjustment capability of the NVM, providing the weight update rule required for neuromorphic computing and pattern classification. Throughout the weight updating process, energy consumption has become a significant metric for eco-friendly development. The energy consumptions of every optical potentiation event and electrical depression event are as low as 3.60×10^{-12} and 1.47×10^{-15} J/μm^2 (Tables S2 and S3 in the ESM), respectively, compared with GaO_x- and ZnO-based neuromorphic devices [4, 59]. Owing to dual-mode functionality SM and NVM

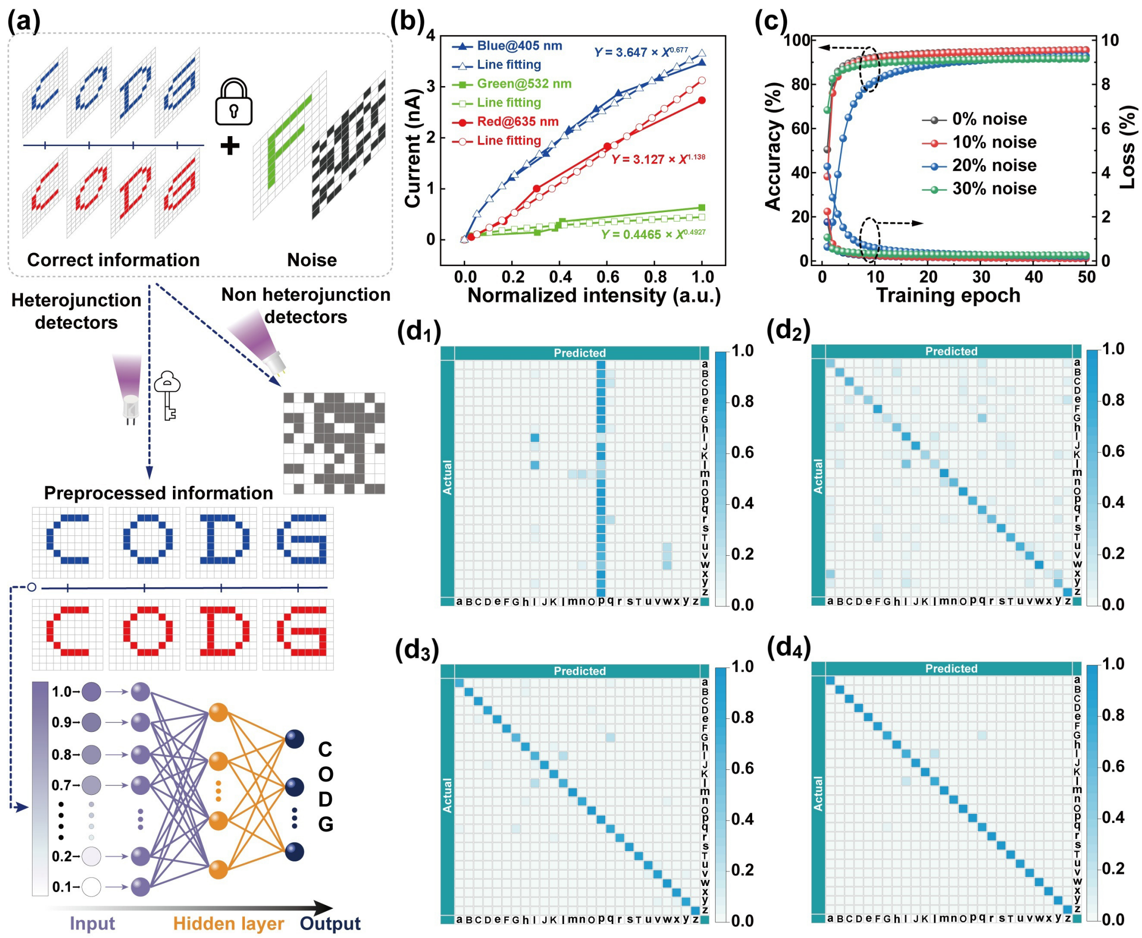

Figure 5 Anti-interference transmission of MNIST digits. (a) The in-sensor processing system with integrates sensing-memory-processing. (b) The distinguishable photoresponse of the $P_{+10\ \mathrm{V}}$-state device under 405, 532, and 635 nm illumination. (c) Recognition accuracy and loss function of MNIST images with different Gaussian noise levels during training. (d) The confusion matrices after different training epochs (1st, 2nd, 10th, and 50th) under 30% noise levels.

within a single neuromorphic device, the in-sensor processing system with integrating sensing-memory-processing has the inherent advantages of simple structure, high efficiency, and low power consumption for digital anti-interference transmission.

Capitalizing on the preprocessing capability of the SM and reconfigurable conductance pathways of the NVM, after 10 training epochs, the recognition accuracy of handwritten digital reach as high as 89.42% and the loss function is as low as 0.33% even when the ratio of noisy pixels is as high as 30%, as shown in Fig. 5(c). Figure S32 in the ESM displays the confusion matrices after 50 training epochs under different noise levels, demonstrating the superior noise robustness of the ANN. With increasing epochs (1st, 2nd, 10th, and 50th) (Fig. 5(d)), the diagonal elements of the confusion matrix become progressively dominant, reflecting that the actual value in each row progressively aligns with the predicted value in each column. The rapid convergence and high noise robustness of the ANN establishes a paradigm for developing low-power and high-efficiency in-sensor processing system. Compared with conventional neuromorphic devices that rely on complex structure, optoelectronic coupling stimulation or multi-wavelength illumination, this monolithic a-GaO_x/HZO heterojunction integrated dual-mode functionalities of SM and NVM is firstly developed by merely modulating single-wavelength light intensity, and offers its significant advantages for integrated sensing-memory-processing in terms of low power consumption, simple device architecture, and high robustness.

3 Conclusion

In summary, inspired by the AVSS paradigm with all-in-one sensing-memory-processing, the dual-mode a-GaO_x/HZO heterojunction neuromorphic device was purposefully designed for integrating SM and NVM. The key-parameter sensitivity and detectivity of the SM are tuned by switchable ferroelectric polarization, thereby enabling two optoelectronic logic gates (i.e., AND and OR). The NVM manifests the dependence of photoresponse excitation and inhibition dynamics on light intensity, adhering to Weber's Law. The fundamental antagonistic photoresponse for visual self-adaptation is further controlled by switchable ferroelectric polarization, implementing fine-tuned regulation of photosensitivity and adaptation index during photopic and scotopic adaptation processes. The integration of both SM and NVM in monolithic a-GaO_x/HZO heterojunction neuromorphic device performs interference pre-filtering and reconfigurable conductance characteristics, allowing for constructing an in-sensor processing system for digital anti-interference communication. Such dual-mode neuromorphic device holds an outstanding promise for advancing next-generation bio-inspired intelligence integrated sensing-memory-processing.

4 Experimental section

4.1 Device fabrication

FTO-coated glass substrates were sequentially ultrasonicated in acetone, ethanol, and deionized water. The a-GaO_x film was deposited on FTO-coated glass substrate via RF magnetron sputtering (100 W, 300 °C, 60 min), by setting the O_2/Ar flow ratio and the working pressure as 1.3/25 and 1.26 Pa, respectively. Subsequently, HZO layer was grown on the sample by thermal-mode atomic layer deposition (ALD-T100B, Hangzhou Jiake Micro-Nano Technology Co., LTD, China) at 300 °C, where deposition cycle ratio of Hf, Zr and H_2O precursor was set as 1:1:4 for controlling Hf, Zr and O element ratio. And then the amorphous HZO layer was performed at 550 °C for 30 s under N_2 atmosphere by using post-deposition rapid thermal annealing (RTA). Finally, Au top electrodes were patterned by ion-sputtering with a shadow mask.

4.2 Characterizations and measurement

Crystalline structures of a-GaO_x and HZO films and a-GaO_x/HZO heterojunction were characterized by XRD (Bruker D8 Advance, Cu Kα radiation) and grazing incidence X-ray diffraction (GIXRD). Cross-sectional microstructure of the a-GaO_x/HZO heterojunction was measured via scanning electron microscopy (SEM, JEOL JSM-7610F Plus). UV–Vis–NIR absorption spectra of a-GaO_x and HZO films and a-GaO_x/HZO heterojunction were acquired using a Cary 5000 spectrophotometer. Chemical states of constituent elements were probed by XPS (AXIS SUPRA+). Surface morphology and roughness were evaluated by AFM (MFP-3D Origin+). Polarization hysteresis loop of HZO film was measured with PFM (MFP-3D Origin+). Photoresponse characteristics of the a-GaO_x/HZO heterojunction device were assessed under 265 nm LED and laser illuminations (360, 405, 532, and 635 nm) using a Keithley 4200A-SCS parameter analyzer.

Electronic Supplementary Material: Supplementary material (Weber's Law; cross-sectional SEM of the a-GaO_x/HZO heterojunction; AFM images of a-GaO_x and HZO films; XRD patterns of a-GaO_x film and a-GaO_x/HZO heterojunction; GIXRD and PFM hysteresis loop of the HZO film; transmission spectra of HZO and a-GaO_x films and a-GaO_x/HZO heterojunction; XPS and UPS patterns of a-GaO_x and HZO films; photoresponse of the heterojunction device; photoresponse of the heterojunction device under different wavelength illumination; photoresponse mechanism of the heterojunction device; temperature fluctuation of the heterojunction device under illumination; the Morse codes for 26 English alphabets programmed by a sequence of light pulses; response time measurement; schematic diagram and Boolean logic definitions of OELGs; schematic diagram of the PD-based photodetection module; schematic diagram of Gaussian noise; LTCP and LTCD behaviors; output confusion matrices of the ANN with 50th epoch under different noise levels; type-II band alignment of the a-GaO_x/HZO heterointerface; and energy consumption of OELGs, every optical potentiation event and every electrical depression event) is available in the online version of this article at https://doi.org/10.26599/NR.2026.94908926.

Data availability

All data needed to support the conclusions in the paper are presented in the manuscript and the Electronic Supplementary Material. Additional data related to this paper may be requested from the corresponding author upon request.

Acknowledgements

This work was supported by the National Natural Science Foundation of China (Nos. 52603447 and 52372107) and the Zhongyuan Talent Program (Talent Cultivation Series) – Leading Talents in Zhongyuan Basic Research, the Henan Center for Outstanding Overseas Scientists (No. GZS2024003). The authors gratefully acknowledge Jun Wan, Hangzhou Jiake Micro-Nano

Technology Co., LTD, China for the instrumental support and technical assistance of the ALD.

Declaration of competing interest

All the contributing authors report no conflict of interests in this work.

Author contribution statement

W. X. H.: Conceptualization (lead), data curation (lead), methodology (lead), formal analysis (lead), investigation (lead), visualization (lead), writing – original draft (lead). J. H. Z: Software (lead), writing – original draft (supporting). Y. J. Z.: Conceptualization (lead), methodology (lead), project administration (lead), writing – review & editing (lead). H. X.: Data curation (supporting), methodology (supporting), formal analysis (supporting). W. Z. H.: Data curation (supporting), methodology (supporting), investigation (supporting). J. R. L.: Methodology (supporting), validation (supporting), supervision (supporting). Q. Q H.: Data curation (supporting), methodology (supporting), investigation (supporting). Y. K. L.: Data curation (supporting), methodology (supporting), formal analysis (supporting). T. Y. W.: Project administration (supporting), validation (lead), supervision (lead). H. W. Z.: Funding acquisition (lead), project administration (lead), supervision (lead), writing – review & editing (lead). All the authors have approved the final manuscript.

Use of AI statement

None.

References

[1] Deng, W. L.; Fan, X. Y.; Du, Y. X.; Ma, S. Y.; Zhang, H. X.; Liu, M. T.; Zhang, H.; Chen, S.; Fu, Q.; Zhang, Y. M. et al. Ultrasensitive and ultrafast self-powered ultraviolet photodetector array for solar-blind and weak-light imaging. *Adv. Mater.* **2026**, *38*, e14968.

[2] Zhou, Y.; Zhang, Z. F.; Yang, X.; Liu, T.; He, G. H.; Lin, C. N.; Huang, W. T.; Liu, H.; Wang, Y.; Wang, Y. N. et al. Solar-blind photodetector arrays fabricated by weaving strategy. *ACS Nano* **2024**, *18*, 7610–7617.

[3] Kim, H. W.; Kim, J. H.; Shin, D. H.; Jung, M. C.; Park, T. W.; Park, H. J.; Han, J. K.; Hwang, C. S. Neuromorphic visual receptive field hardware with vertically integrated indium-gallium-zinc-oxide optoelectronic memristors over silicon neuron transistors. *Adv. Mater.* **2026**, *38*, e13907.

[4] Cui, D. S.; Pei, M. J.; Lin, Z. H.; Zhang, H.; Kang, M. Y.; Wang, Y. F.; Gao, X. X.; Su, J.; Miao, J. S.; Li, Y. et al. Versatile optoelectronic memristor based on wide-bandgap Ga_2O_3 for artificial synapses and neuromorphic computing. *Light: Sci. Appl.* **2025**, *14*, 161.

[5] Wen, J. C.; Li, B. Q.; Ren, L.; Wang, K. Y.; Cao, Y. J.; Ren, L. Q. Biomimetic additive manufacturing tactile sensing systems: Mechanisms, materials, techniques, and prospects. *Mater. Today* **2026**, *92*, 711–750.

[6] Jiang, Q. Y.; Wang, K. K.; Wang, F.; Leu, K.; Li, R.; Zhao, Y. L.; Xi, A. K.; Zang, Y. L.; Zhang, R. F. High-performance photodetectors based on suspended ultralong carbon nanotubes. *ACS Nano* **2024**, *18*, 25249–25256.

[7] Min, L. L.; Sun, H. X.; Guo, L. Q.; Wang, M.; Cao, F. R.; Zhong, J.; Li, L. Frequency-selective perovskite photodetector for anti-interference optical communications. *Nat. Commun.* **2024**, *15*, 2066.

[8] Tian, R. J.; Zhang, Y.; Ji, Y. K.; Li, C.; Wu, X. H.; Wang, J. G.; Jia, S. W.; Liu, L.; Zhang, M. W.; Zhang, Y. et al. On-chip graphene photodetectors with a nonvolatile *p-i-n* homojunction. *Light: Sci. Appl.* **2025**, *14*, 238.

[9] Xu, J. K.; Zhang, Y. X.; Wang, J. L.; Zhang, W. F.; Li, T. Y.; Zhang, K. S.; Yan, X. B. Ultra-low power and robust Bi_2SeO_5 films optoelectronic memristors for bio-visual perception computing systems. *Adv. Mater.* **2025**, *37*, 2509174.

[10] Wang, S. J.; Chen, X.; Zhao, C.; Kong, Y. X.; Lin, B. J.; Wu, Y. Y.; Bi, Z. Z.; Xuan, Z. Y.; Li, T.; Li, Y. X. et al. An organic electrochemical transistor for multi-modal sensing, memory and processing. *Nat. Electron.* **2023**, *6*, 281–291.

[11] Zhu, J. X.; Sun, B. R.; Xi, M. X.; Zhan, Y. F.; Zhang, B.; Zhu, Y. L. Flexible electronics in humanoid five senses for the era of artificial intelligence of things (AIOT). *Mater. Today* **2025**, *88*, 1066–1086.

[12] Alqahtani, B.; Kumbhar, D.; Syed, A. M.; Hasan Raza Ansari, M. D.; Li, H. R.; Dominguez, K.; Pal, P.; Albagami, M.; Kumar, D.; Alvarado, A. et al. Smart multifunctional memory devices capable of sensing: The role of responsive materials in advancing nonvolatile memories. *Mater. Today* **2025**, *90*, 563–597.

[13] Wang, Y.; Zhou, T.; Cui, Y.; Xu, M. Y.; Zhang, M.; Tang, K.; Chen, X. R.; Tian, H. X.; Yin, C. J.; Huang, J. W. et al. Reconfigurable sensing-memory-processing and logical integration within 2D ferroelectric optoelectronic transistor for CMOS-compatible bionic vision. *Adv. Funct. Mater.* **2024**, *34*, 2400039.

[14] Sebastian, A.; Le Gallo, M.; Khaddam-Aljameh, R.; Eleftheriou, E. Memory devices and applications for in-memory computing. *Nat. Nanotechnol.* **2020**, *15*, 529–544.

[15] Qu, S. D.; Sun, L. M.; Xu, H. H.; Zhu, Q. S.; Cheng, Y.; Du, X. X.; Yuan, Y. M.; Ye, X.; Gu, F.; Xu, W. T. A flexible neuromorphic window capable of in-sensor computing and self-adaptive color regulation. *Adv. Funct. Mater.* **2026**, *36*, e15967.

[16] Dang, B. J.; Sun, K. X.; Su, H. X.; Chen, J. X.; Yao, P. Y.; Zeng, T.; Shi, S.; Zhou, G. W.; Liu, L.; Xu, X. H. et al. HZO/HSO superlattice ReFET array integrating optical sensing for neuromorphic vision computing. *Adv. Mater.* **2025**, *37*, e08889.

[17] Huang, H. Y.; Liang, X. P.; Wang, Y. Y.; Tang, J. S.; Li, Y. K.; Du, Y. W.; Sun, W.; Zhang, J. N.; Yao, P.; Mou, X. et al. Fully integrated multi-mode optoelectronic memristor array for diversified in-sensor computing. *Nat. Nanotechnol.* **2025**, *20*, 93–103.

[18] Li, D. L.; Zhou, M. T.; Gong, Y. N.; Zhao, W. Y.; Sun, H. L.; Tang, J.; Zhang, Y. P.; Wang, G. P. 1D van der Waals superlattices for polarization-sensitive photodetectors. *Adv. Mater.* **2025**, *37*, 2508035.

[19] Tsarev, S.; Proniakova, D.; Liu, X. Q.; Wu, E. F.; Matt, G. J.; Sakhatskyi, K.; Ferraresi, L. L. A.; Kothandaraman, R.; Fu, F.; Shorubalko, I. et al. Vertically stacked monolithic perovskite colour photodetectors. *Nature* **2025**, *642*, 592–598.

[20] Zhang, Y.; Chang, K.; Yan, H. L.; Huang, C. H.; Nomura, K. Artificial solar-blind optosynapses using amorphous gallium oxide phototransistors for optical in-sensor neuromorphic applications. *ACS Nano* **2025**, *19*, 35401–35413.

[21] Cao, F.; Hu, Z. J.; Yan, T. T.; Hong, E. L.; Deng, X. L.; Wu, L. M.; Fang, X. S. A dual-functional perovskite-based photodetector and memristor for visual memory. *Adv. Mater.* **2023**, *35*, 2304550.

[22] Luo, L. L.; Huang, H.; Yang, L.; Hao, R.; Hu, X. L.; Li, Y. T.; Zhao, X. L.; Zhang, Z. M.; Long, S. B. Ultra-fast gallium oxide solar-blind photodetector with novel thermal pulse treatment. *Adv. Mater.* **2025**, *37*, 2414130.

[23] Kim, B.; Kim, J. Y.; Yang, D.; Park, S. H.; Ryu, J. E.; Lee, Y. J.; Kim, H. J.; Bae, J.; Kim, J.; Park, Y. et al. Self-powered ultraviolet-C imaging using epitaxial gallium oxide membranes with anisotropic domain conduction. *ACS Nano* **2025**, *19*, 22870–22881.

[24] Liu, Y.; Hou, X. H.; Ding, M. F.; Xu, Z. H.; Yu, S. J.; Zhao, X. L.; Xu, G. W.; Zhou, X. Z.; Long, S. B. Tunable superlinear gallium oxide gate-all-around deep-ultraviolet phototransistor for near-field imaging. *ACS Nano* **2025**, *19*, 33174–33183.

[25] Feng, S. Y.; Li, J. X.; Feng, L. Z.; Liu, Z. T.; Wang, J. C.; Cui, C.; Zhou, O. X.; Deng, L. J.; Xu, H. N.; Leng, B. et al. Dual-mode

conversion of photodetector and neuromorphic vision sensor via bias voltage regulation on a single device. *Adv. Mater.* **2023**, *35*, 2308090.
[26] Kim, W.; Kim, H.; Yoo, T. J.; Lee, J. Y.; Jo, J. Y.; Lee, B. H.; Sasikala, A. A.; Jung, G. Y.; Pak, Y. Perovskite multifunctional logic gates via bipolar photoresponse of single photodetector. *Nat. Commun.* **2022**, *13*, 720.
[27] Laswick, Z.; Wu, X. H.; Surendran, A.; Zhou, Z. L.; Ji, X. D.; Matrone, G. M.; Leong, W. L.; Rivnay, J. Tunable anti-ambipolar vertical bilayer organic electrochemical transistor enable neuromorphic retinal pathway. *Nat. Commun.* **2024**, *15*, 6309.
[28] Ying, H. T.; Xie, K. H.; Cai, H. C.; Li, Z. S.; Liu, L.; Guo, X. D.; An, M. H.; Shang, H. P.; Zheng, X. R. Multifunctional logic-in-memory circuits based on reconfigurable WSe_2 transistors via enhanced ambipolarity. *ACS Nano* **2025**, *19*, 19442–19453.
[29] Li, W.; Mu, T. H.; Li, P. S.; Zhang, S. Y.; Sun, P. C.; He, J. B.; Hu, X. Y.; Wang, Y. C.; Gan, X. T.; Wang, S. X. Reconfigurable floating-gate devices with ambipolar $ReSe_2$ channel: Dual-mode storage, NMOS-PMOS transformation, logic functions, synapse simulations, positive and negative photoconductive effects. *Adv. Funct. Mater.* **2025**, *35*, 2425359.
[30] Wang, Y. Y.; Jiang, Y. H.; Wu, J. B.; Zhu, Z. K.; Zeng, Y.; Yu, P. P.; Li, G. H.; Guan, Q. W.; Li, H.; Xu, L. J. et al. Multi-axial broadband photopyroelectric response in biaxial perovskite ferroelectric crystals driven by the Ferro-pyro-phototronic effect. *Adv. Funct. Mater.* **2025**, *35*, 2505521.
[31] Gong, G. D.; Zhou, Y.; Xiong, Z. Y.; Sun, T.; Li, H. X.; Li, Q. X.; Zhao, W. Y.; Zhang, G. H.; Zhai, Y. B.; Lv, Z. Y. et al. An antagonistic photovoltaic memristor for bioinspired active contrast adaptation. *Adv. Mater.* **2024**, *36*, 2409844.
[32] Liao, F. Y.; Zhou, Z.; Kim, B. J.; Chen, J. W.; Wang, J. L.; Wan, T. Q.; Zhou, Y.; Hoang, A. T.; Wang, C.; Kang, J. F. et al. Bioinspired in-sensor visual adaptation for accurate perception. *Nat. Electron.* **2022**, *5*, 84–91.
[33] Shi, L.; Shi, K.; Zhang, Z. C.; Li, Y.; Wang, F. D.; Si, S. H.; Liu, Z. B.; Lu, T. B.; Chen, X. D.; Zhang, J. Flexible retinomorphic vision sensors with scotopic and photopic adaptation for a fully flexible neuromorphic machine vision system. *SmartMat* **2024**, *5*, e1285.
[34] Tan, Z. H.; Wang, Y. Z.; Shao, L.; Li, S. Q.; Hao, L.; Cao, Y. H.; Chen, J. W.; Zhong, W. K.; Dong, S.; Yang, X. Y. et al. Bias-switchable dual-mode organic photodetectors for spectrally adaptive vision and secure encoding. *Mater. Today* **2025**, *90*, 343–352.
[35] Luo, D. G.; Kefalov, V.; Yau, K. W. Phototransduction in rods and cones. *Senses: A Compr. Ref.* **2008**, *1*, 269–301.
[36] Fain, G. L.; Matthews, H. R.; Cornwall, M. C.; Koutalos, Y. Adaptation in vertebrate photoreceptors. *Physiol. Rev.* **2001**, *81*, 117–151.
[37] Kim, J. S.; Gaggio, B.; Bakhit, B.; Lenzi, V.; Marques, L.; Fairclough, S. M.; Strkalj, N.; Choe, D. H.; Silva, J. P. B.; MacManus-Driscoll, J. L. Reducing coercive field and improving endurance in ferroelectric epitaxial $Hf_{0.5}Zr_{0.5}O_2$ thin films via novel interface layer approach. *Adv. Sci.* **2026**, *13*, e17314.
[38] Shang, Z. X.; Liu, L. C.; Wang, G. C.; Xu, H.; Cui, Y. Y.; Deng, J. M.; Lou, Z.; Yan, Y. Z.; Deng, J. X.; Han, S. T. et al. Ferroelectric polarization enhanced optoelectronic synaptic response of a $CuInP_2S_6$ transistor structure. *ACS Nano* **2024**, *18*, 30530–30539.
[39] Wang, Y. F.; Zeng, Z. X. S.; Tian, Z. Q.; Li, C.; Braun, K.; Huang, L. Y.; Li, Y.; Luo, X. Y.; Yi, J. L.; Wu, G. C. et al. Sliding ferroelectricity induced ultrafast switchable photovoltaic response in ε-InSe layers. *Adv. Mater.* **2024**, *36*, 2410696.
[40] Jiang, Y. R.; Xu, Y. Z.; Wang, Y.; Yu, L. M.; Zhang, S. C.; Li, X. P.; Song, X. H.; Jiang, C.; Xia, C. X. Nonvolatile operation of bioinspired spectral-adaptive transistor with ferroelectric-photosensitive gate. *ACS Nano* **2025**, *19*, 32471–32481.
[41] Zhang, X. L.; Hong, E. L.; Tan, X. J.; Liu, J.; Jiang, A. Q.; Fang, X. S. 2D ruddlesden-popper perovskites/PVDF-TrFE photodetector for anti-interference vision system derived from ferroelectric polarization modulation. *Adv. Funct. Mater.* **2025**, *35*, 2424848.
[42] Zheng, Z. Y.; Qiao, B. S.; Han, Z. P.; Qiu, J.; Yao, Y. F.; Shu, C.; Liu, Y. J.; Hu, H.; Xu, Y.; Yu, B. et al. Multi-defect-engineering in ZNO/GO heterostructures for optoelectronic synaptic devices with ultra-high dynamic range and low energy consumption. *InfoMat* **2026**, *8*, e70089.
[43] Kwon, O.; Lee, D. H.; Oh, S.; Yoon, J.; Kim, H. B.; Ahn, J. H.; Park, W.; Kim, H. S.; Cho, B. Dynamic control of synaptic plasticity by competing ferroelectric and trap-assisted switching in IGZO transistors with Al_2O_3/HfO_2 dielectrics. *Adv. Funct. Mater.* **2026**, *36*, e13449.
[44] Ding, K.; Zhang, H.; Jiang, J. L.; Luo, J. S.; Wu, R. L.; Ye, L. J.; Tang, Y.; Pang, D.; Li, H. L.; Li, W. J. Balancing carrier dynamics in oxygen-vacancy-tuned amorphous Ga_2O_3 thin-film self-powered photoelectrochemical-type solar-blind photodetector arrays for underwater imaging. *Adv. Sci.* **2024**, *11*, 2407822.
[45] Yao, J.; Wang, Q. N.; Geng, L.; Zhao, Z. X.; Zhao, Y. Y.; Teng, Y.; He, Y. Q.; Zhang, Y.; Li, Q.; Qiu, S. et al. Gate-tunable highly linear bipolar photoresponse in Se@SWCNT adaptive neurons for dynamically programmable neuromorphic computing. *Adv. Mater.* **2025**, *37*, e06367.
[46] Jang, S.; Soh, K.; Lee, C.; Nam, T.; Jang, M.; Park, J. I.; Lee, C.; Choi, J.; Yoon, J. H.; Im, S. G. A unipolar-driven synaptic transistor for environment-adaptable vision system. *Nat. Commun.* **2025**, *16*, 7636.
[47] Xiong, Z. S.; Liang, W.; Zhang, M. Y.; Mao, D. C.; Xia, Q. F.; Xu, G. Y. Parallelizing analog in-sensor visual processing with arrays of gate-tunable silicon photodetectors. *Nat. Commun.* **2025**, *16*, 4728.
[48] Xu, H.; Liu, B.; Xin, L.; Hou, W. X.; Li, Y. K.; Peng, W. B.; Han, Q. Q.; Zhang, Y. Z.; Zhang, Y. J.; Zheng, H. W. Enabling bipolar photoresponse improvement of a-$GaO_x/Hf_{0.5}Zr_{0.5}O_2$ heterojunction self-powered solar-blind photodetector by coupling Ferro-pyro-phototronic effect. *Appl. Phys. Rev.* **2025**, *12*, 041422.
[49] Dan, H. Y.; Li, H. Y.; Xu, L.; Guo, C.; Bowen, C. R.; Yang, Y. Light induced photovoltaic and pyroelectric effects in ferroelectric $BaTiO_3$ film based schottky interface for self-powered and flexible multi-modal logic gates. *InfoMat* **2024**, *6*, e12531.
[50] Chai, B.; Shi, K. M.; Wang, Y. L.; Liu, Y. J.; Liu, F.; Zhu, L.; Huang, X. Y. Integrated piezoelectric/pyroelectric sensing from organic-inorganic perovskite nanocomposites. *ACS Nano* **2024**, *18*, 25216–25225.
[51] Dang, P. P.; Zhang, T.; Liu, Z. H.; Sun, S. Y.; Wang, Y.; Zhang, F.; Wang, K. X.; Pan, X. H.; Lu, B.; Zhu, L. P. et al. Tunable pyro-phototronic effect by polar interface engineering in Ga_2O_3. *Adv. Funct. Mater.* **2025**, *35*, 2504294.
[52] Tan, Y. F.; Qiao, Q.; Zhao, T. G.; Chang, S. L.; Zhang, Z. F.; Zang, J. H.; Lin, C. N.; Shang, Y. Y.; Yang, X.; Zhou, J. W. et al. Gallium oxide nanocrystals for self-powered deep ultraviolet photodetectors. *J. Mater. Sci. Technol.* **2024**, *190*, 200–209.
[53] Lu, Y.; Miranda Cortez, P. A.; Tang, X.; Liu, Z. Y.; Khandelwal, V.; Krishna, S.; Li, X. H. κ/β-Ga_2O_3 type-II phase heterojunction. *Adv. Mater.* **2025**, *37*, 2406902.
[54] Hou, X. H.; Zhao, X. L.; Zhang, Y.; Zhang, Z. F.; Liu, Y.; Qin, Y.; Tan, P. J.; Chen, C.; Yu, S. J.; Ding, M. F. et al. High-performance harsh-environment-resistant GaO_x solar-blind photodetectors via defect and doping engineering. *Adv. Mater.* **2022**, *34*, 2106923.
[55] Li, Y. Q.; Guan, Z. Y.; Zhang, Y. J.; Wang, J. T.; Liu, B.; Han, Q. Q.; Xu, H.; Zheng, H. W.; Li, X. G. Ferroelectric polarization modulated photodetection-synaptic integration functions of a-$GaO_x/Bi_{0.85}La_{0.15}FeO_3$ semiconductor-ferroelectric heterojunction. *ACS Photonics* **2024**, *11*, 4966–4977.
[56] Lee, M. J.; Kim, T. H.; Lee, S. H.; Oh, S.; Khan, M. A.; Lee, G. M.; Choi, Y. K.; Lee, S.; Ahn, H.; Oh, S. J. et al. Intermediate layer-assisted trap density reduction in low-power optoelectronic

memristors for multifunctional systems. *Adv. Funct. Mater.* **2025**, *35*, 2421080.
[57] Bahrawy, A.; Galek, P.; Gellrich, C.; Niese, N.; Mohamed, M. A. A.; Hantusch, M.; Grothe, J.; Kaskel, S. Nanostructured H–WO_3-Based ionologic gates with enhanced rectification and transistor functionality. *ACS Nano* **2025**, *19*, 20655–20671.
[58] Kuang, J. H.; Liu, K.; Liu, M. H.; Shao, M. C.; Zhu, M. L.; Liu, G. C.; Wen, W.; Chen, J. Y.; Qin, M. C.; Pan, Z. C. et al. Interface defects tuning in polymer-perovskite phototransistors for visual synapse and adaptation functions. *Adv. Funct. Mater.* **2023**, *33*, 2209502.
[59] Cheng, Z. P.; Wang, T. L.; Zhu, J. Y.; He, Y. Q.; Liu, S. J.; Li, M. Y.; Lu, H. F.; Wen, X. Y.; Lee, J.; Liu, S. S. et al. All-inorganic lead-free $Cs_2AgBiBr_6$/ZnO artificial retina synapse based on photoelectric synergistic dual-mechanism for neuromorphic computing. *Small* **2025**, *21*, 2411129.